Experimental and numerical investigation of the energy harvesting flexible flag in the wake of a bluff body

Usman Latif[1], Chaudary Abdullah[1], Emad Uddin[*1], M. Yamin Younis[2],
Muhamad Sajid[1], Samiur Rehman Shah[1] and Aamir Mubasha[3]

[1]Department of Mechanical Engineering, SMME, National University of Sciences and Technology (NUST),
H-12, Islamabad, 46000, Pakistan
[2]Department of Mechanical Engineering, Mirpur University of Science and Technology (MUST), Mirpur 10250 (AJK), Pakistan
[3]Mechanical Engineering Program, Middle East Technical University Northern Cyprus Campus, Mersin, Turkey

Abstract. Inspired by the energy harvesting eel, a flexible flag behind a D-shape cylinder in a uniform viscous flow was simulated by using the immersed boundary method (IBM) along with low-speed wind tunnel experimentation. The flag in the wake of the cylinder was strongly influenced by the vortices shed from the upstream cylinder under the vortex-vortex and vortex-body interactions. Geometric and flow parameters were optimized for the flexible flag subjected to passive flapping. The influence of length and bending coefficient of the flexible flag, the diameters (*D*) of the cylinder and the streamwise spacing between the cylinder and the flag, on the energy generation was examined. Constructive and destructive vortex interaction modes, unidirectional and bidirectional bending and the different flapping frequency were found which explained the variations in the energy of the downstream flag. Voltage output and flapping behavior of the flag were also observed experimentally to find a more direct relationship between the bending of the flag and its power generation.

Keywords: immersed boundary method; fluid-structure interaction; energy harvesting eel; piezoelectric flag

1. Introduction

The interaction of the vortex and the flexible flag in wake of a bluff body is a common occurrence in nature and in engineering fields. The limited availability and the environmental impact of fossil fuels motivate the development of renewable energy sources. Considerable efforts are focused on the use of renewable energy from natural resources such as flowing water, rain, tides, wind, sunlight, geothermal heat and biomass. Renewable energy from small-scale hydro, modern biomass, wind, solar, geothermal and biofuels accounted for global energy consumption was 2.7% in 2008, increased to 5.8% in 2012 and is growing rapidly (Arthouros 2014).

From a hydrodynamic point of view, experimental evidence has supported the assertion that the appropriate synchronization of the positioning of the flag in the wake of the bluff body can be advantageous due to wake interactions resulting in significant energy harvesting (Allen and Smits 2001, Barrero-Gil *et al.* 2010, Bernitsas *et al.* 2008, Peng and Zhu 2009, Singh *et al.* 2012). Nevertheless, the phenomenon of the hydrodynamic interactions of a flag in the wake of a bluff body has not yet well understood, and a more detailed understanding of the mechanisms would be desirable.

Aquatic animals utilize oscillatory motions of the fins or wings to achieve propulsion and maneuvering

(Triantafyllou *et al.* 2004). They extract energy from the incoming vortices or unsteady flows (Zhu *et al.* 2002). The caudal fin of a fish can absorb energy from the vortices shed from the dorsal fins to increase the propulsion efficiency (Zhu *et al.* 2002), moreover, dead fish is capable of moving upstream within the Karman vortex street generated by a D-shape cylinder (Liao *et al.* 2003). Bio-inspired energy harvesting devices based on the oscillatory motion of foils had been developed by using an oscillating wing to extract energy from the unsteady flow fields generated by the free-surface waves. The application of the flapping wings to extract energy from uniform flows was first proposed by McKinney and De Laurier (McKinney and DeLaurier 1981). Both experiments and theoretical analyses showed that a foil submerged in the free surface could propel by using the energy from the incoming waves (Grue *et al.* 1988, Isshiki and Murakami 1984, Wu and Chwang 1975, Wu 1971). With the growing importance of renewable energy, the interest in this novel concept has been rekindled in the past few years. Allen and Smits (Allen and Smits 2001) examined the response of the piezoelectric membrane to vortex shedding. The direct numerical simulation has been performed and for a dimple-shaped object at low Reynolds number, the drag is found to be increased (Ge 2016). A focus pattern of a vibrating flexible filament in a viscous fluid was reported by Xu *et al.* (2018). They showed that the focus pattern of the vibrating filament and the corresponding wall attraction phenomenon are mainly caused by the balance between the joint force on the filament and the pressure from the flow field. The vortex-induced vibrations (VIV) has recently gained a lot of attention in harvesting energy from tidal or low head

---

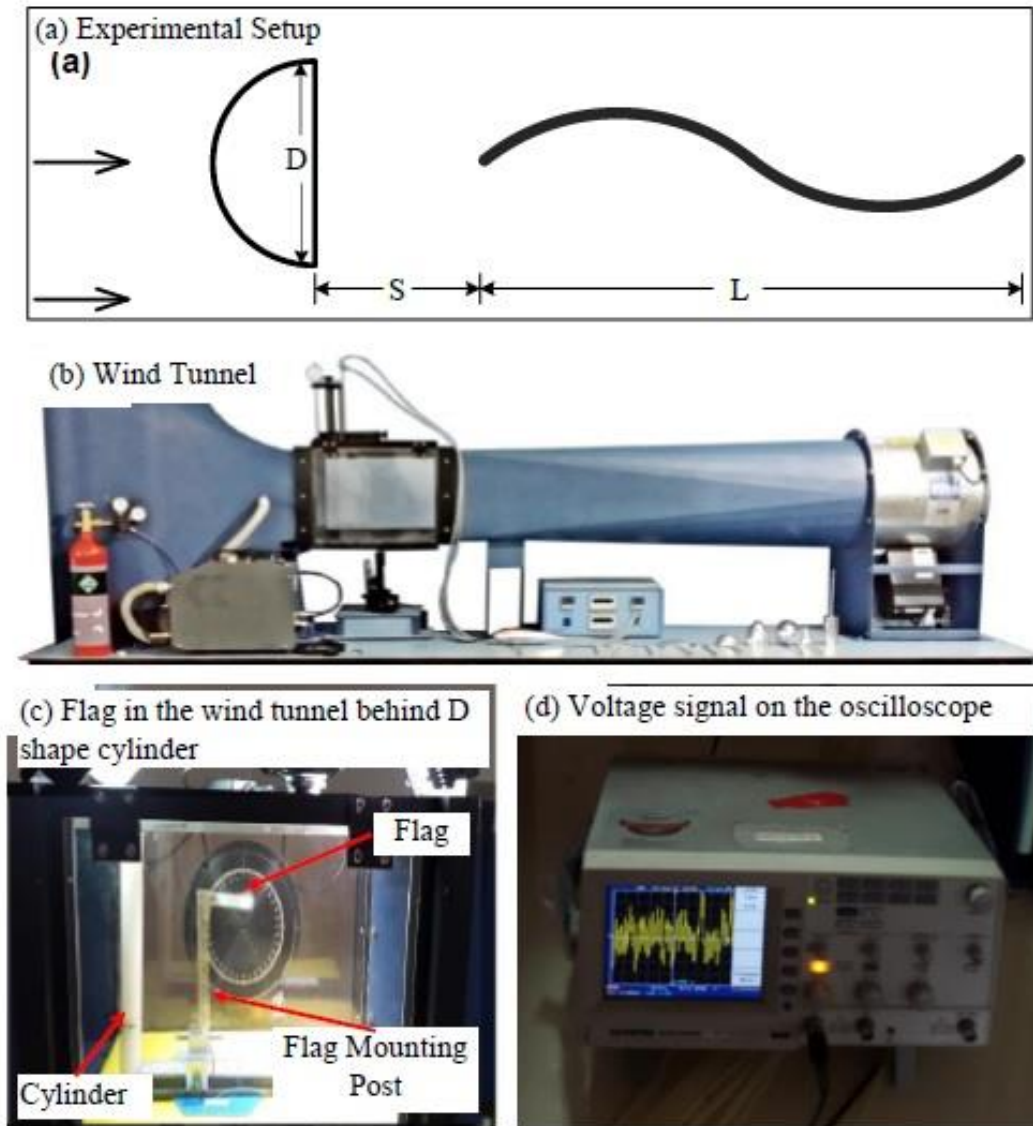*Corresponding author, Dr.
 E-mail: emaduddin@smme.nust.edu.pk

Fig. 1 (a) Schematic, (b)Wind tunnel, (c) Test section and (d) Voltage measurement

streams. The most known idea under this category is to attach a cylinder at the end of a piezoelectric cantilever beam (termed as energy harvester). The alternate Karman vortex shedding exerts unsteady aerodynamic forces on the piezoelectric sheet. When the vortex shedding frequency synchronizes with the natural frequency of the energy harvester, the resonant transverse vibrations occurs (Baz and Ro 1991, Dai *et al*. 2014) termed as Vortex Induced Vibrations. Different modes of VIV can be obtained depending on the varying mass-damping parameter (Govardhan and Williamson 2004, Kalak and Williamson 1997). Galloping (Abdelkefi 2016, Hartong 1984) of prismatic cylinders (rectangular, square and D-shaped etc.) and wake galloping (Matsumoto 2005, Matsumoto *et al*. 2006, Bin *et al*. 2017) (when the energy harvester as described above is placed behind another bluff body) can also be used to extract the VIV based energy.

The current study provides the dynamics of flow around a flexible flag (eel) in the wake of a D-shaped cylinder subjected to a two-dimensional uniform viscous flow. The flexible flag is subjected to passive flapping. The introduction of a flapping flexible flag in the downstream of a D-shaped cylinder imparts more complicated interaction phenomenon. There are some analytical and numerical studies on the energy harvesting eel but the detail investigation and optimization of the parameters is the missing link (Eldredge 2008). This study provides necessary insights towards a better understanding of the dynamics of the flapping flexible flag in the wake of the D-shaped cylinder subjected to viscous flow and the parametric optimization. The dependence of the energy generated by the variation in the stream-wise gap distance between the D-shaped cylinder and the downstream flag, the length and the bending rigidity of the downstream flag were examined in detail. This study provides the intriguing

results: within a range of the flapping conditions, the flapping downstream flag can experience a distinct drag enhancement thus producing more energy. Moreover, the vortices shed by the D-shaped cylinder interact with the downstream flag via two modes of interaction for passive flapping i.e., constructive and destructive modes, which explains the significant drag changes experienced by the flexible structures. In the next section the formulation of the problem, numerical method and experimental method are briefly described. In Section 3, the results and discussion are presented. Finally, conclusions are drawn in Section 4.

2. Problem formulation

2.1 Numerical methodology

A flexible flag in the wake of a D-shaped cylinder was subjected to the two-dimensional viscous flow. A schematic diagram of the geometric configuration and the coordinate system is shown in Fig. 1.

The distance between the D-shaped cylinder and the flexible flag was varied by adjusting the stream-wise gap distance '*S*'. The head of the downstream flag was fixed under a simply supported boundary condition and the boundary condition for the free end was considered at the tails. The rigid D-shaped cylinder is placed at the center (0, 0) with diameter '*D*'. The fluid domain was defined by an Eulerian coordinate system, and a separate Lagrangian coordinate system was applied to the flexible flag. The flexible flag in a viscous flow was modeled using an improved immersed boundary method (Huang *et al.* 2007) in which the governing equations of the fluid flow and the flexible flag were solved in each coordinate system, and the interactions among components were calculated using a feedback law.

The fluid motion was governed by the incompressible Navier-Stokes and continuity Eqs.

$$\frac{\partial \boldsymbol{u}}{\partial t} + \boldsymbol{u} \cdot \nabla \boldsymbol{u} = -\nabla p + \frac{1}{\mathrm{Re}} \nabla^2 \boldsymbol{u} + \boldsymbol{f} , \qquad (1)$$

$$\nabla \cdot \boldsymbol{u} = 0, \qquad (2)$$

where $\boldsymbol{u}$ is the velocity vector, p is the pressure, $\boldsymbol{f}$ is the momentum force applied to enforce the no-slip conditions along the immersed boundary, and the Reynolds number *Re* is defined by $\mathrm{Re} = \rho_0 U_\infty L / \mu$, with ρ_0 the fluid density, U_∞ the free stream velocity, *L* the flag length, and μ the dynamic viscosity.

The flag motion was governed by

$$\frac{\partial^2 \boldsymbol{X}}{\partial t^2} = \frac{\partial}{\partial s} \left(T \frac{\partial \boldsymbol{X}}{\partial s} \right) - \frac{\partial^2}{\partial s^2} \left(\gamma \frac{\partial^2 \boldsymbol{X}}{\partial s^2} \right) - \boldsymbol{F} \qquad (3)$$

where *s* denotes the arc length, $\boldsymbol{X} = \boldsymbol{X}$ (*s,t*) the position, *T* the tension force, γ the bending rigidity and $\boldsymbol{F}$ the Lagrangian force exerted on the flexible flag by the fluid.

Eq. (3) was non-dimensionalized by the flag density r_1, the flag length *L*, and the free stream velocity U_∞. It should be pointed out that the tension force can be determined from the inextensibility condition of flag (Huang *et al.* 2007), and the bending rigidity is defined as *EI*, with *E* the Young's modulus and *I* the second moment of area, which gives the non-dimensional value *γ*. The boundary conditions applied at the fixed end and the free end were

$$\boldsymbol{X} = \boldsymbol{X}_0, \quad \frac{\partial^2 \boldsymbol{X}}{\partial s^2} = (0,0) \quad \text{for the fixed end} \qquad (4)$$

$$T = 0, \frac{\partial^2 \boldsymbol{X}}{\partial s^2} = (0,0), \quad \frac{\partial^3 \boldsymbol{X}}{\partial s^3} = (0,0) \quad \text{for the free end.} \quad (5)$$

The interaction force between the flow and the structure was calculated using the feedback force by the relation

$$\boldsymbol{F} = \alpha \int_0^t \left(\boldsymbol{U}_{ib} - \boldsymbol{U} \right) d\tau + \beta \left(\boldsymbol{U}_{ib} - \boldsymbol{U} \right) \qquad (6)$$

where α and β are large negative free constants -10^5 and -10^3, respectively in Huang *et al.* (2007), $\boldsymbol{U}_{ib}$ is the fluid velocity obtained by interpolation at the immersed boundary, and $\boldsymbol{U}$ is the velocity of the flag expressed by $\boldsymbol{U} = d\boldsymbol{X}/dt$. On the other hand, $\boldsymbol{X}_{ib}$ and $\boldsymbol{U}_{ib}$ denote, respectively, the position and velocity of the immersed boundary, which were determined using the local Eulerian fluid velocity, as expressed by

$$\boldsymbol{U}_{ib}(s,t) = \int_\Omega \boldsymbol{u}(\boldsymbol{x},t)\delta(\boldsymbol{X}(s,t) - \boldsymbol{x})d\boldsymbol{x} \qquad (7)$$

where $\delta(\ )$ denotes a smoothed approximation of the Dirac delta function, and Ω_f is the fluid region. Eq. (8) provides an interpolation of the Eulerian fluid velocity at the Lagrangian points. In physics, Eqs. (6) -(8) represent a stiff spring system. This system connected the Lagrangian points on the immersed boundary to the surrounding fluid particles. After obtaining the Lagrangian force $\boldsymbol{F}$, the expression was transformed to the Eulerian form using the smoothed Dirac delta function,

$$\boldsymbol{f}(\boldsymbol{x},t) = \frac{\rho_1}{\rho_0 L_r} \int_\Gamma \boldsymbol{F}(s,t)\delta(\boldsymbol{x} - \boldsymbol{X}(s,t))ds \qquad (8)$$

where $r = r_1 / (r_0 L)$, based on the non-dimensionalization steps, and Ω_s denotes the structure region. After discretization, the force was applied over a width of several grids, which supported the smoothed delta function.

The overall computational process, in which the present numerical algorithm was used to simulate the fluid–flexible body interactions, is summarized as follows:

(1) Initialize the computation parameters, the meshes, and the fluid and solid motions; set $\boldsymbol{X}_{ib}^0 = \boldsymbol{X}^0$.

(2) At the *n*th time step, the fluid velocity $\boldsymbol{u}^n$ and the solid position $\boldsymbol{X}^n$ and velocity $\boldsymbol{U}^n$ are known. Interpolate the fluid velocity at the Lagrangian points to obtain $\boldsymbol{U}_{ib}^n$, and calculate the positions of the immersed boundary points $\boldsymbol{X}_{ib}^n$. Then calculate the Lagrangian momentum force $\boldsymbol{F}^n$.

(3) Map the Lagrangian momentum force onto the Eulerian grid. Obtain the updated fluid velocity field and pressure field.

(4) Substitute $\boldsymbol{F}^n$ into the flag motion equation and obtain the flag position at the new time step $\boldsymbol{X}^{n+1}$, as well as the velocity $\boldsymbol{U}^{n+1} = (\boldsymbol{X}^{n+1} - \boldsymbol{X}^n)/\Delta t$. Return to step 2 and march to the next time step.

The computational domain for the fluid flow ranged from -2 to 6 in the stream-wise (*x*) direction and from -4 to 4 in the span-wise (*y*) direction, both of which directions were normalized by the flag length. The Eulerian grid size for the fluid was 512 × 350 in the stream-wise and span-wise directions, respectively, and the Lagrangian grid size for each flag was 64. The Eulerian grid was uniformly distributed along the *x*-direction, and it was uniform in the *y*-direction for -2 ≤ *y* ≤ 2, but stretched otherwise. The far-flow field was applied at the top and bottom boundaries as well as the inlet of the fluid domain, whereas the convective boundary condition was used at the outlet. The computational time step was set to 0.0002, which resulted in a CFL number of 0.1. The validation of the flow solver employing the immersed boundary method, as well as the structure solver for the flag motion, has been provided in Huang *et al.* (2007).

2.2 Experimental setup

Experiments were conducted in an open loop, suction type wind tunnel as shown in Fig. 1. The wind tunnel had a cross-section of 300 mm × 300 mm and was capable of producing free-stream velocity *U* between 1 ms^{-1} to 20 ms^{-1}.

The leading edge of the piezo flag was clamped with a vertical rod of the diameter 2 mm. while the trailing edge is free. The piezoelectric flag (Piezoelectric Polymer Vibration Sensor, LDT1-028K, Measurement Specialties, Inc.,) had an active length of 60 mm and a width of 12 mm. Flag motion was observed using a slow-motion camera (Sony RX-100 IV) mounted at the top of the test section for wind speeds varying from 5ms^{-1} to 10ms^{-1}. An oscilloscope (Gwinstek GDS-2062) was connected to the piezoelectric flag to visualize and store wave form of the voltage produced due to flag motion. To enhance the visualization of the flag motion; the test section was illuminated by two LED lights (Mcopus TTV204). The maximum blockage ratio of less than 8% was observed in all the tests conducted. Behaviors of flag motion and voltage produce were recorded behind two cylinders of different diameters by varying velocity and distance to diameter ratio i.e., *S/D*.

2.3 Variation in Reynolds number

Two different Reynolds numbers 300 and 30,000 were used for computational and experimental analyses. Small *Re* (= 300) for simulation was selected owing to the inclusion of the three-dimensional effects for the *Re* > 300 (Johnson and Patel 1999). As the phenomenon was at the low speed and the numerical simulations were performed in two dimensional, so the Reynolds number of 300 was selected. Also in our previous work, the Reynolds number of 300 was used, because of the same constraints (Uddin *et al.* 2015, Uddin *et al.* 2013, Uddin and Sung 2011).

The experimentation was conducted in a low-speed wind tunnel, the velocity range was between 1 to 12 ms^{-1}, resulting in the maximum Reynolds number of 30,000 at 12 ms^{-1}. If Re_D is less than around 3.8×10^5, the boundary layer remains laminar from the stagnation point at the front of the cylinder to the point where it separates. The resulting flow pattern, termed sub-critical, is associated with a high drag on the cylinder, C_d being about 1.2. (Panton 2005, van Dyke 1982) The flow attachment to the cylinder remains laminar for both *Re*=300 and 30,000. Above the critical Reynolds number around $Re = 3.8 \times 10^5$ the near-wake recirculation region shrinks considerably, the drag coefficient decreases and periodic vortex shedding is no longer able to be detected (Taneda 1978). The dominant flow features at both Reynolds numbers are quite similar. The Reynolds number of 30,000 was selected for the wind tunnel experimentation owing to the wind tunnel limitations, similar flow features and laminar boundary layer below the critical Reynolds number of around 3.8×10^5.

3. Results and discussion

3.1 Numerical results

A schematic diagram of the problem setup and the coordinate system for the downstream flag in the wake of the D-shaped cylinder subjected to a uniform flow is plotted in Fig. 1. The computational configurations were set to be the same as described in section 2.1. The initial position of the downstream flag was parallel with the stream-wise direction with its leading edge located at a stream-wise distance of '*S/D*' from the origin. The downstream flag was inclined at an angle of 0.1π relative to the streamwise direction. Even if the inclination angle was changed to -0.1π, the results obtained after several transient flapping periods remained unchanged. The flow patterns were investigated by conducting simulations over a long time period between 100 and 200 flapping periods. The flow patterns obtained after a minimum of 20 flapping periods were analyzed. The flow patterns and interaction forces were characterized in terms of the energy generated from the bending motion of the flag (E_b). The total potential energy is given by Zhu (2009)

$$E = E_S + E_B, \tag{9}$$

where E_S and E_B are the stretching energy and the bending energy, respectively.

$$E_s = \frac{1}{2} K_s \int \left(\sqrt{\frac{\partial X}{\partial X_{ib}} \frac{\partial X}{\partial X_{ib}}} - 1 \right)^2 dX_{ib}, \tag{10}$$
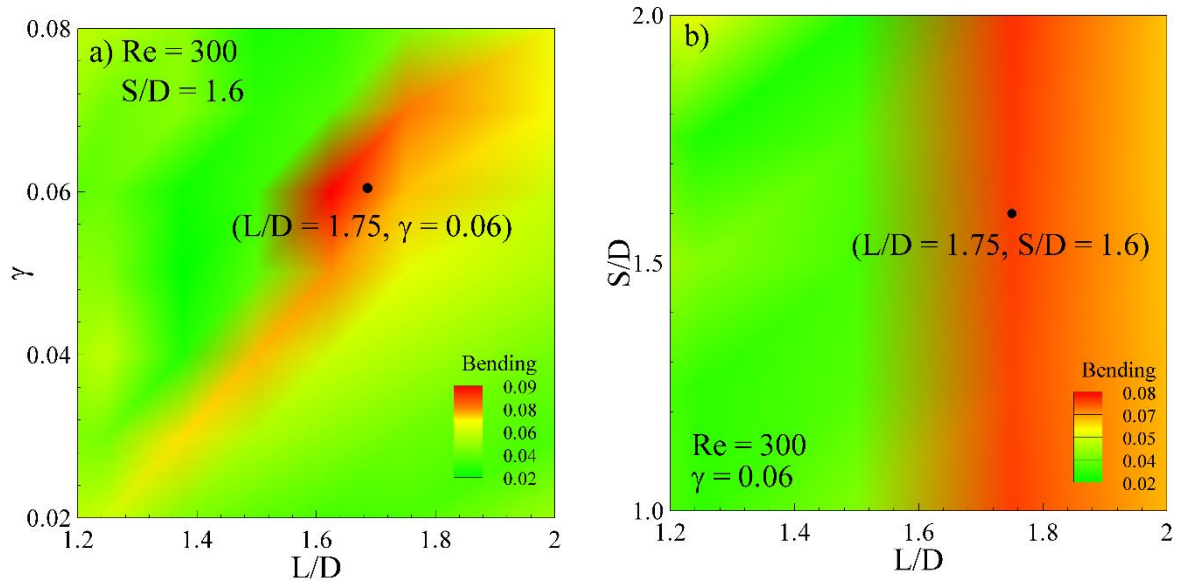
Fig. 2 Contours of the bending energy for different (a) *L/D* and *γ*, (b) *L/D* and *S/D*

$$E_B = \frac{1}{2} K_B \int \frac{\partial^2 X}{\partial X_{ib}^2} \frac{\partial^2 X}{\partial X_{ib}^2} dX_{ib}, \qquad (11)$$

where K_S and K_B are the stretching coefficient and bending coefficient of the flag, respectively. The major contribution in the total potential energy is from the bending energy, the bending energy was therefore shown in the subsequent plots. As reported by the Tian *et al.* (2011), the potential energy due to the stretching is very less, they showed the significant reduction in the potential energy as compared to the kinetic energy. The electric equations were not discussed because of the direct measurement of the electric voltage from the flag deformation. Shoele and Mittal (2016) followed the electrical coupling strategy of the Michelin and Doare (2013) based on the potential flow. They assumed that the output electric circuit is coupled to the deformation of the flag through mutual interaction between the electric voltage of the patches, local stretch or compression of the patches as a result of the beam deflection and charge transfer through the thickness of the flag. They expressed the coupling in which the electric voltage is directly proportional to the flag deformation (Michelin and Doare 2013). The results obtained from the Shoele and Mittal (2016) showed that, for the eel with head fixed, the maximum amplitude and power coefficient have direct a relationship to each other (both remain almost the same for the given range), but for the inverted flag, the power coefficient is not directly related to the maximum amplitude owing to the low dominant frequency and flapping behavior. A quantitative characterization of the interaction behavior was supplemented by qualitative evaluations of the flag deformations and the vorticity contours within the flow, which provided an intuitive understanding of the vortex–flexible body interactions.

Three parameters were chosen for optimization within the following ranges: the streamwise gap distance between the D-shaped cylinder and the downstream flag ($1 \leq S/D \leq 2$), the bending coefficient of the flag ($0.02 \leq \gamma \leq 0.08$) and the length of the flag ($1.2 \leq L/D \leq 2.0$).The bending energy E_b of the downstream flag as a function of the length and the bending coefficient of the flag is plotted in Fig. 2(a).

The *Re* = 300 and *ρ* = 1 are used unless otherwise stated. For a fixed streamwise gap distance of *S/D* = 1.6 (Fig. 2(a)), the bending energy contours clearly mark two regions, one representing the maximum bending energy in the range of $1.5 \leq L/D \leq 1.9$ for $0.04 \leq \gamma \leq 0.075$, and the second region representing the low bending energy is constituted by all the remaining *L/D* and *γ* values. The high bending energy region has four times energy than the low bending energy region. The details of the variation in the bending energy with the change in the length and the bending rigidity can be unfolded by analyzing the evolution of the tail position and the flag deformation shapes (Fig. 3), the power spectrum (Fig. 4) and the vorticity diagram (Fig. 5). Four points corresponding to the low and high bending energy are shown for different *L/D* ratio and *γ*.

Figs. 3(a) and 3(b) shows the tail position evolution and flag deformation shapes with an increase in the bending rigidity from 0.020 to 0.060 for the same *L/D* ratio. The tail position evolution shows the increase in the flapping frequency (seven peaks in 30 seconds as compared to six peaks) with the increase in the bending rigidity. It is accompanied by the change in the flag deformation shape, the flag deformation shape remains constrained at increased bending coefficient (Fig. 3(b) as compared to the low bending coefficient (Fig. 3(a)) by the virtue of the more stiffened flag.
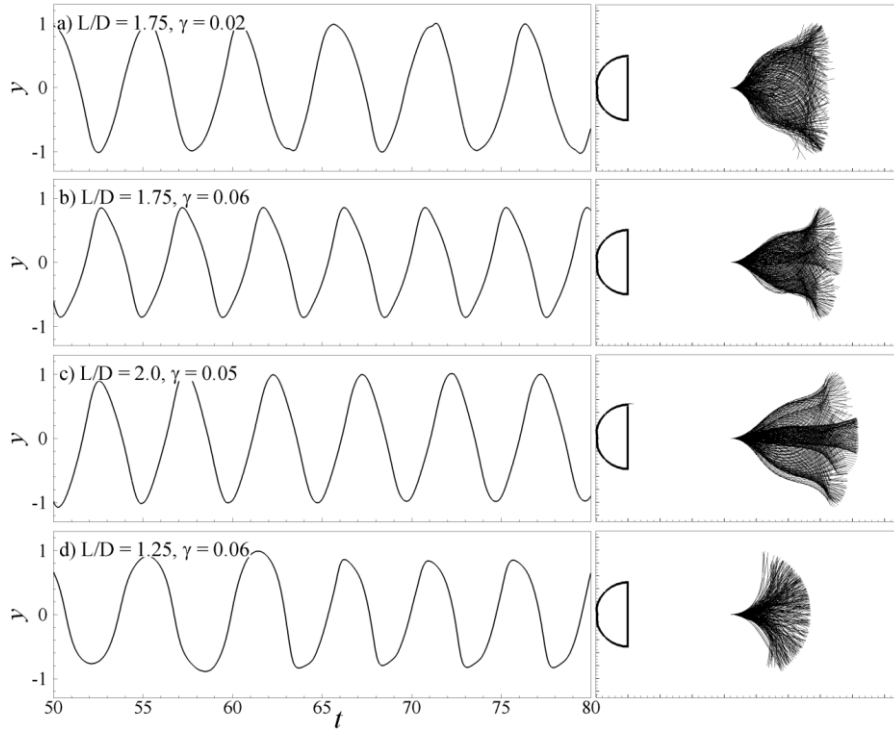
Fig. 3 Evolutions of the tail position and corresponding flag deformations for different L/D and γ
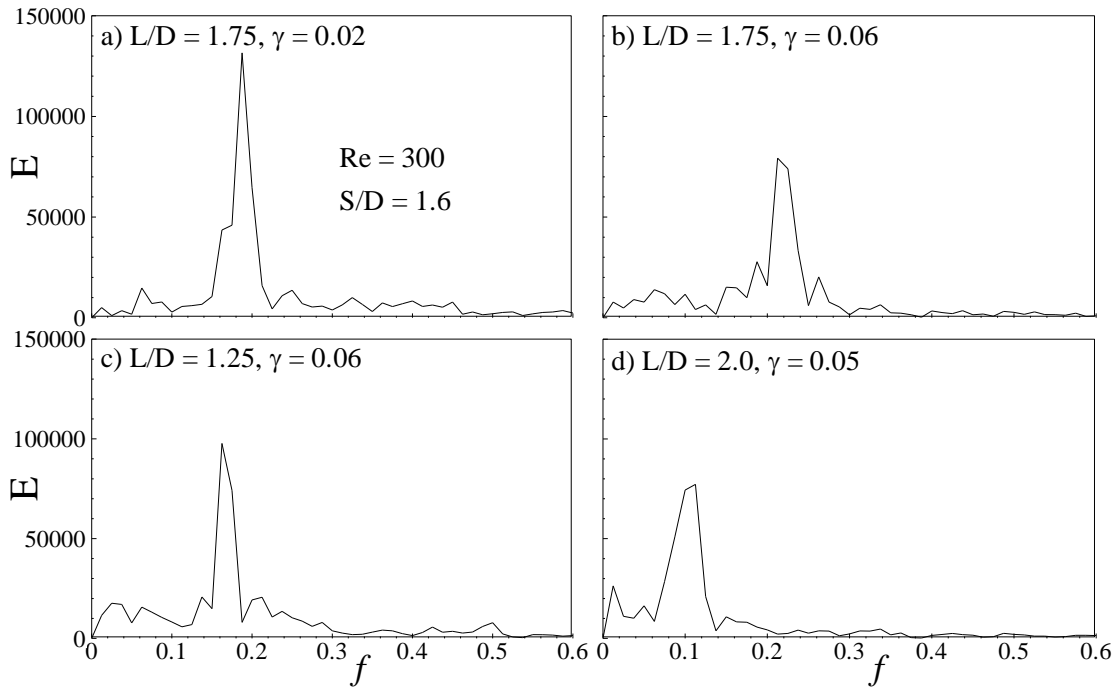

Fig. 4 Power spectra for different L/D and γ

The power spectra of the corresponding two cases are shown in Figs. 4(a) and 4(b). With the increase in the stiffness of the flag, the dominant frequency of the flag is increased from 0.19 to 0.22. For the lesser flexible flag in Figs. 3 and 4(a), the flag gets significant deformation by the influence of the upstream vortices, this changes the flag shape significantly, resulting in decreasing the dominant frequency. The increase in the stiffness in Figs. 3 and 4(a) causes more resistance to the upstream vortices, which decreases the influence of the upstream vortices resulting in the low deformation of the flag as well as an increase in the dominant frequency which is near the natural frequency of
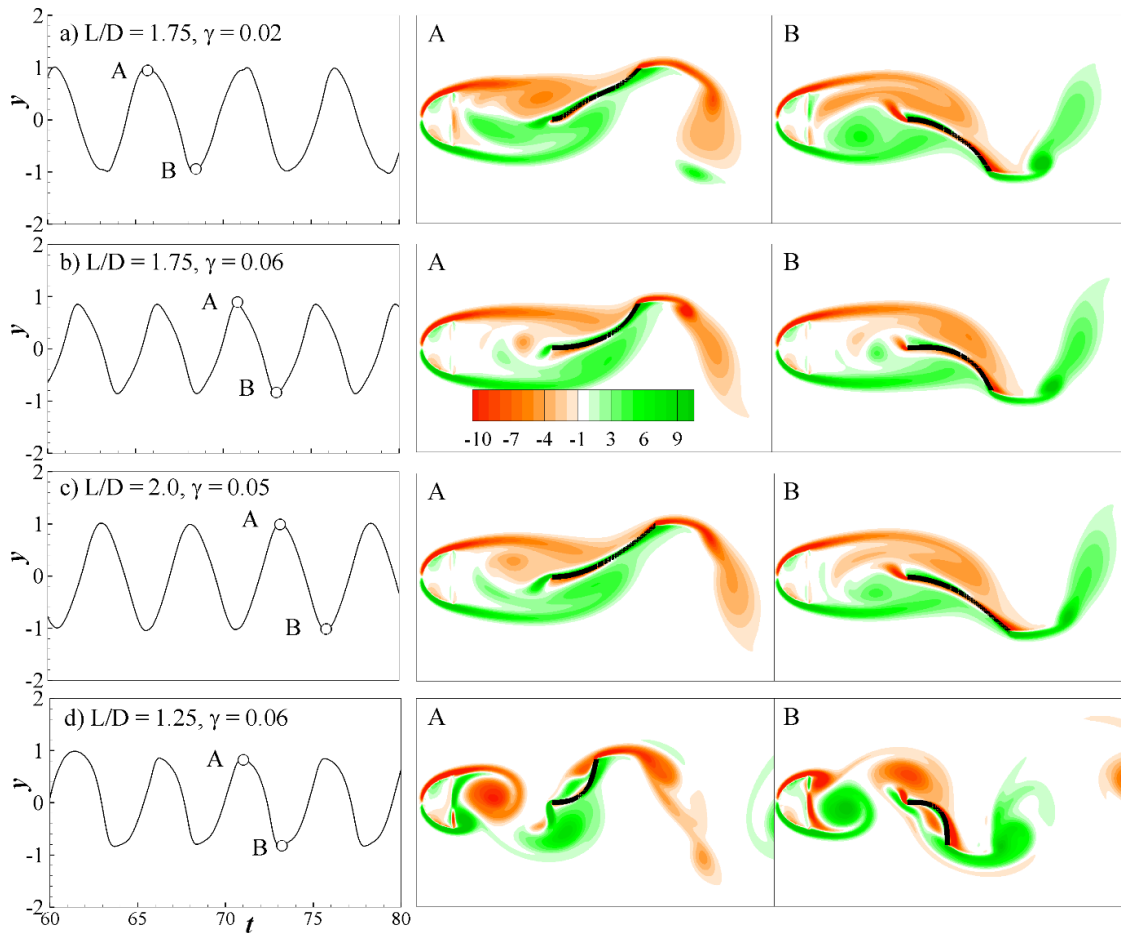
Fig. 5 Contours of vorticity for different L/D and γ

the flag in a uniform flow. The length of the flag is increased to *L/D* = 2.0 and the bending stiffness *γ* = 0.05, the bending energy is low while the flag deformation is significant (Fig. 3(c)) and the flapping frequency is lower than the high bending energy region. As the *L/D* is decreased to 1.25 and the bending rigidity is increased to 0.06, the increased stiffness and the length have combined effect on the form of unidirectional curvature bending (Fig. 3(d)) and the flapping frequency is similar to low bending energy region. The power spectrum of these two low bending region points shows that the dominant frequency is lower than the high bending energy case. With the decrease in the length of the flag (*L/D* from 2 to 1.25) and increase in bending stiffness (*γ* = 0.05 to 0.06), the flag deformation curvature switches from bi-curvature to the unidirectional curvature bending with higher dominant frequency (Figs. 4 (c) and 4(d)).

The vorticity contours are shown in Fig. 5, the flag is in the shear layer generated by the D-shaped cylinder for the length ratio above *L/D* = 1.5. For the length below 1.5, the flag effects the upstream vortices by increasing the shear resistance to the upstream vortices which delays/blocks the upstream vortices and causes the two vortices to combine and create a shear layer for the downstream flag, while for the flag with reduced length and at the same streamwise gap distance, the vortices are completely shed from the D-

cylinder which interacts with the flag in the constructive manner where the positive vortices on the lower-side of the D-shaped cylinder interacts with the positive vortices (lower-side) of the flag, similarly negative vortices shed from the upper side of the cylinder interacts with the upper side (negative vortices) of the flag. This effect is the same for all the cases as the constructive mode is dependent on the gap distance (Kim *et al.* 2010). The creation of the shear layer causes suction zone in front of the downstream flag. Beal *et al.* (2006) reported the suction zone for the *S/D* < 2.0, and this study reveals that apart from the gap distance, it is also dependent on *L/D* by the virtue of increased shear resistance. The suction region creates the extra force on the flag which is higher for *L/D* = 1.75 and *γ* = 0.06 shown by the absence of the vorticies in front of the flag while for the other cases (Figs. 5(a) and 5(c)) the presence of vortices in front of the flag causes lower effect on the suction zone resulting in the low bending energy. The map on the *γ - L/D* plane (Fig. 2(a)) gives the optimal *L/D* = 1.75 and *γ* = 0.06 for maximum energy harvesting.

Fig. 2(b) showed the bending energy surface plot between the length of the flag and the gap distance between the cylinder and the flag. Details are shown in the tail position evolution, the power spectrum and the vorticity flow field (Figs. 6-8).
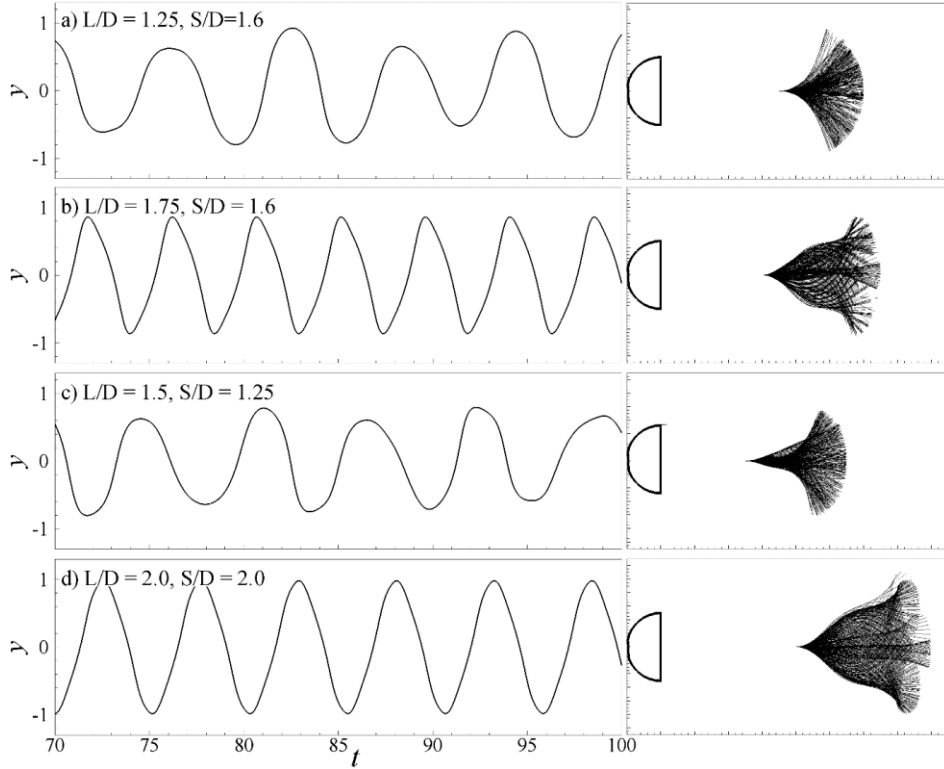
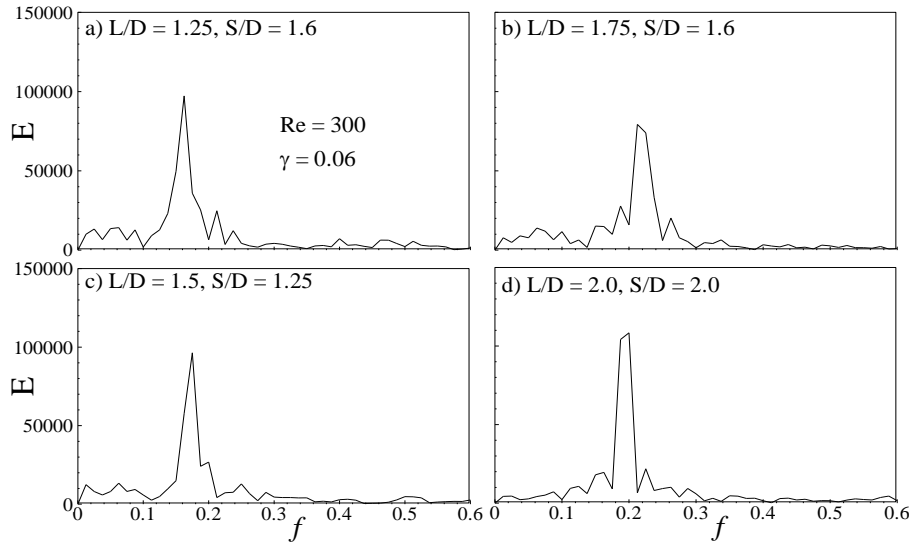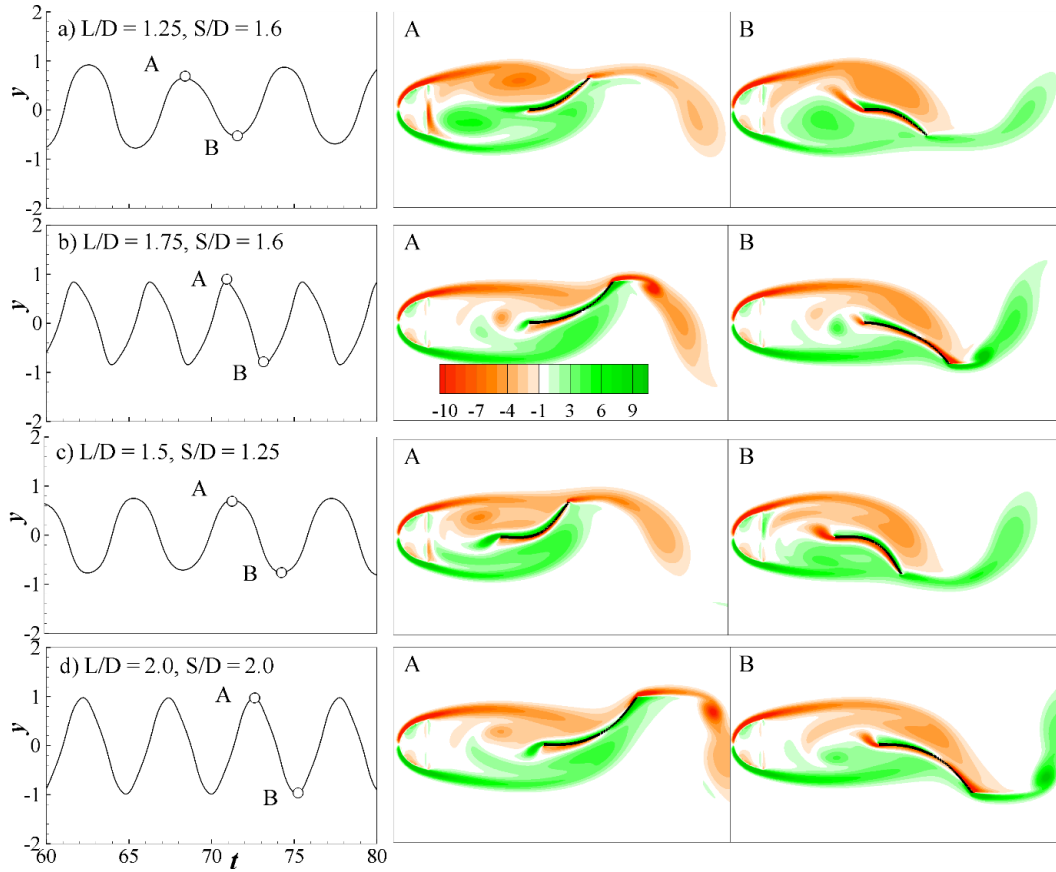Fig. 6 Evolutions of the tail position and corresponding flag deformations for different L/D and S/D
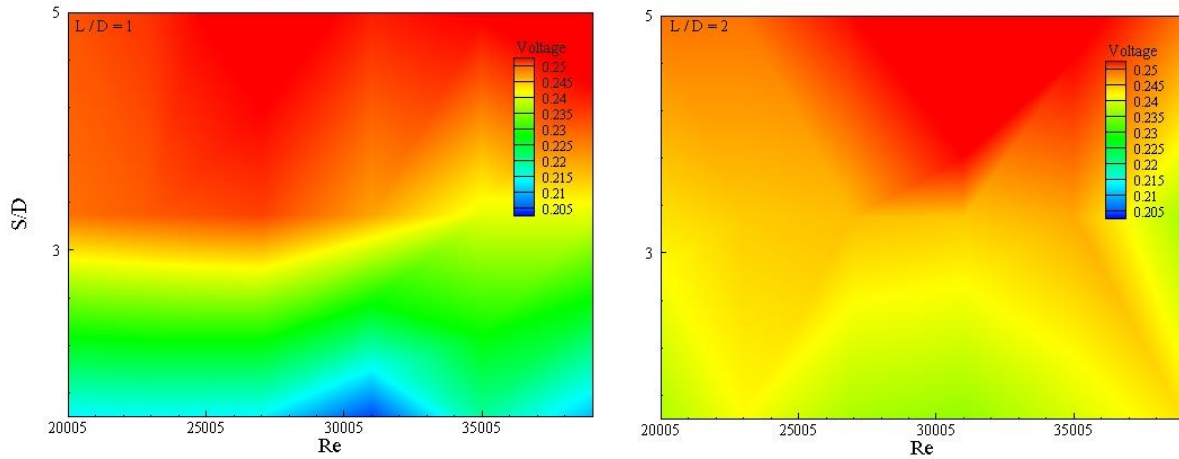

Fig. 7 Power spectra for different L/D and S/D

The tail position evolution shows the lowest energy region at *L/D* = 1.25, *S/D* = 1.75 (Fig. 7(a)) which corresponds to the lowest dominant frequency (f = 0.15). The increase in the bending energy is accompanied by the increase in the dominant frequency (Figs. 7(c) and 7(d)). The maximum dominant frequency of f = 0.22 is observed for *L/D* = 1.75, *S/D* = 1.75 (Fig. 7(b)). The tail position evolution shows the two interesting findings, 1) the

frequency of the tail (Fig. 8) at the optimal location (Figs. 7 and 8(b)) has higher values. 2) Unidirectional curvature deformation of the flag is observed for *L/D* < 1.75 (Figs. 8(a) and 8(c)), while for *L/D* > 1.75, there is bidirectional curvature deformation (Figs. 8(b) and 8(d)). The unidirectional/constrained deformation is attributed to the low bending energy. For fixed *γ* and *S/D*, variations in *L/D* cause a jump from unidirectional to bidirectional curvature

Fig. 8 Contours of vorticity for different L/D and S/D

Fig. 9 Contours of Electric Energy for different Reynolds number and *S/D* at (a) *L/D* = 1 and (b) *L/D* = 2

deformation (Figs. 8(a) and 8(b)) which shows that the curvature change is a function of the length of the flag. For fixed γ, the shorter flag length causes constrained motion, as the shorter flag length results in less effective area for exertion of the viscous forces by the fluid. Increasing the length to *L/D* = 1.75 provides sufficient surface area of the flag to exert more viscous forces on the flag to cause the bidirectional curvature flapping. The vorticity field (Fig. 8) shows the vortex interaction with the flag for *L/D* = 1.25,

S/D = 1.6 (Fig. 8(a)) while for the other length and streamwise distances there is a shear layer and suction zone (Figs. 8(b)-8(d)). No vortices in front of the high bending energy zone (Fig. 8(b)) compared to the vortices in the suction zone show the effect of the suction zone on the bending energy. This map (Fig. 2(b)) gives the optimal length and the gap distance for maximum energy harvesting (*L/D* = 1.75, *S/D* = 1.75) while optimal bending rigidity is γ = 0.06.
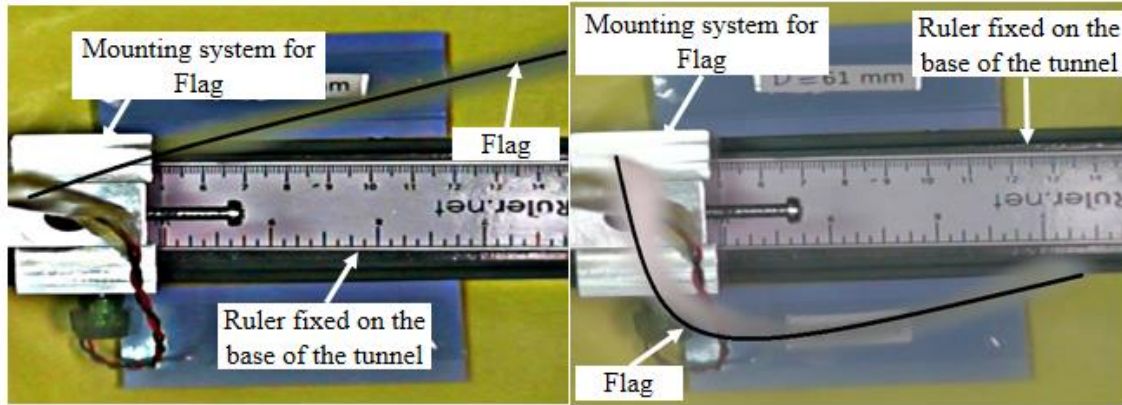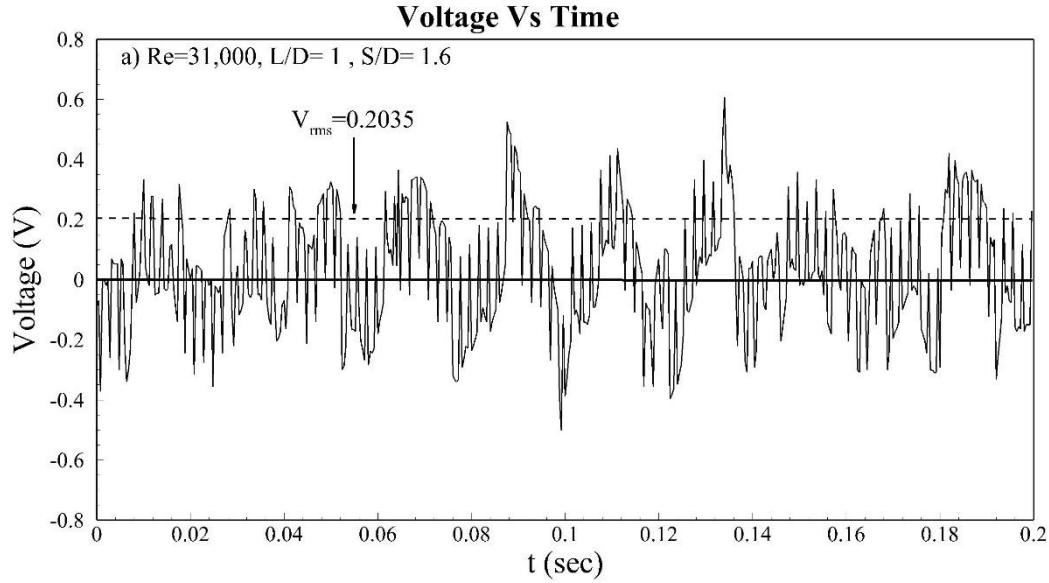
Voltage Vs Time

a) Re=31,000, L/D= 1 , S/D= 1.6

V_{rms}=0.2035

Fig. 10 Voltage graph along with flag behavior for *L/D*=1, *S/D*=1.6
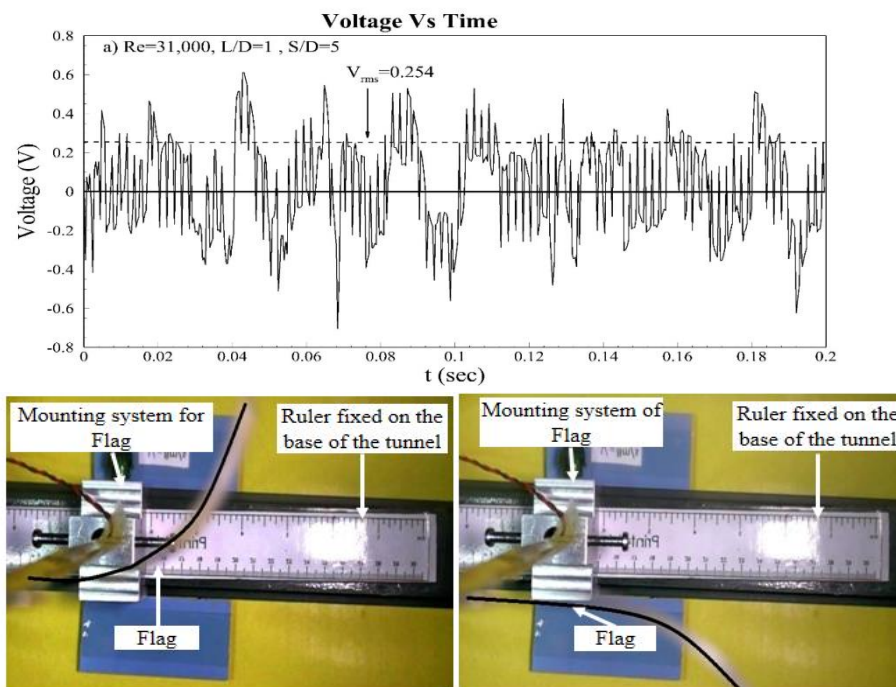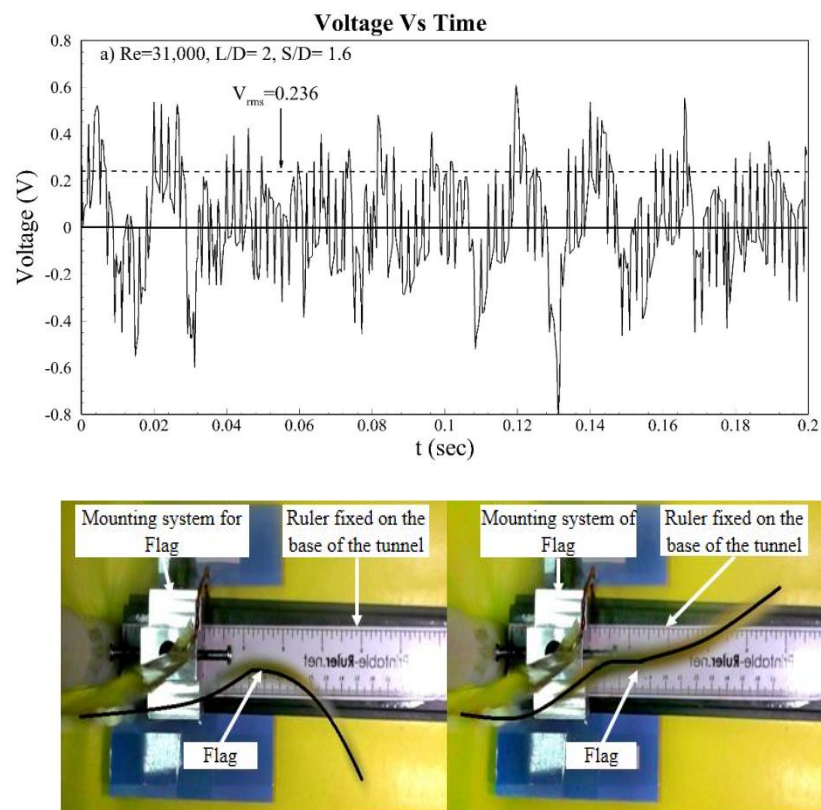
3.2 Effect of variation in Reynolds number

There is a difference in fluid flow physics as the Reynolds number is changed from 300 in the simulation to 30,000 in the experimentations, the flow at the *Re*=300 is characterized as the unsteady planar-symmetric regime while *Re*=30,000 is characterized as the turbulent wake regime. The flow at *Re*=300 is the transition to unsteady wake consisting of the periodic shedding of a series of interconnected vortex loops and the flow exhibits planar symmetry. While at *Re*=30,000 the flow has the vortex loops which continue to be shed in a more irregular manner, although strong periodic fluctuations still exist in the wake.

The increase in the Reynolds number increases the irregular vortex shedding but the strong periodic shedding similar to the low Reynolds number exists. This makes the two *Re* comparable in terms of periodic vortex shedding, while the Strouhal number increases from 0.14 to 0.2 (Sakamoto and Haniu 1990). Above the critical Reynolds number around $Re = 3.8 \times 10^5$ the near-wake recirculation region shrinks considerably, the drag coefficient decreases

sharply, and periodic vortex shedding is no longer able to be detected experimentally (Taneda 1978). Hence the Strouhal number is not significantly affected while the periodic fluctuations remain the same for both Reynolds numbers.

3.3 Experimental results

In experimentation, because of physical constraints and wind tunnel limitations, all the parameters as used in the simulation cannot be achieved, only the *L/D* and *S/D* were kept similar to those in the simulations. Experimentation is done by varying *Re* values from 25,000 to 35,000, *S/D* from 1 to 5 and *L/D* from 1 to 2. For a fixed *L/D* = 1 (Fig. 9(a)), the voltage contours clearly mark two regions, one representing the maximum voltage in the range of $3.0 \leq S/D \leq 5$ for $25,000 \leq Re \leq 30,000$. For the suction/incomplete vortex shedding region (S/D < 3), the voltage generated by the deforming piezoelectric flag is lower. As the gap distance is increased (*S/D* > 3), the voltage becomes higher, while for the low Reynolds number simulations, the bending energy is independent of the gap distance for *S/D* <

Fig. 11 Voltage graph along with flag behavior for *L/D*=1, *S/D*=5

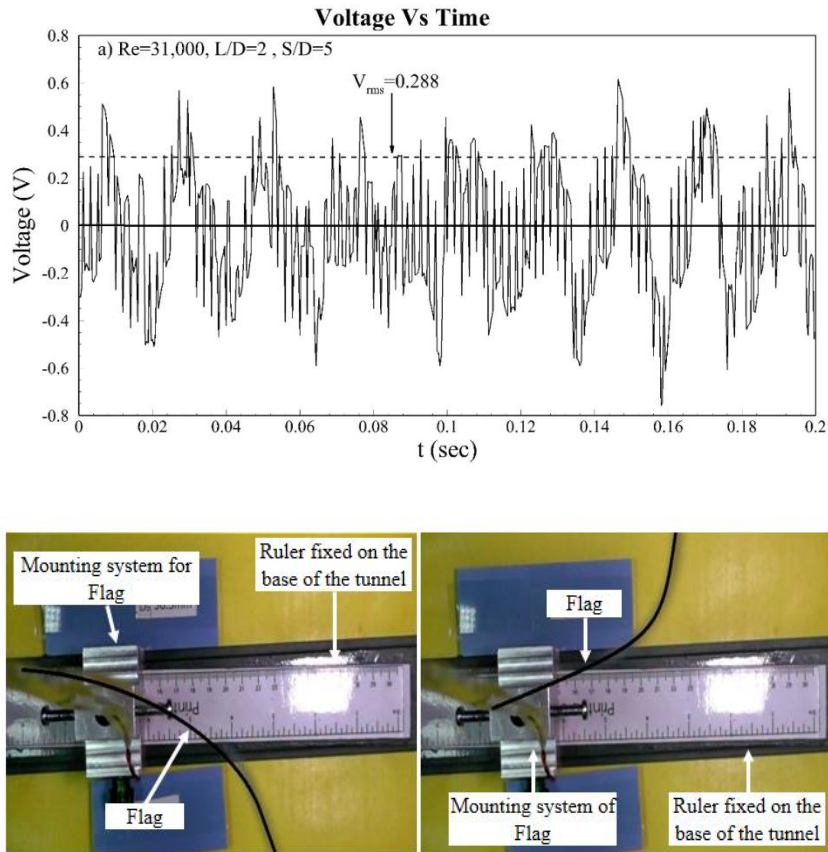Fig. 12 Voltage graph along with flag behavior for *L/D*=2, *S/D*=1.6

Fig. 13 Voltage graph along with flag behavior for *L/D*=2, *S/D*=5

3. The second region representing the low voltage was constituted by all the remaining *S/D* and *Re* values. The voltage produced in the high voltage region was 21% more than the low voltage region (Fig. 9(b)). *L/D* = 2 also shows a similar behavior, i.e. maximum voltage production region was observed at S/*D* ≥ 3.0 and 25,000 ≤ *Re* ≤ 35000 while low voltage region was observed at all the remaining *S/D* and *Re* values. Minimum voltage in the low voltage region was increased by 15% when doubling the flag length. With the increase in *L/D* from 1 to 2, it was observed that high voltage region begins to expand. At *L/D* = 1 high voltage region was found more concentrated toward *Re* = 25,000 while at *L/D* = 2 it moves toward Re = 30,000 and spreads till *Re* = 35,000. At *L/D* =1, lower zone value obtained is 0.20V while at *L/D* = 2 lower zone value increases to 0.225V which shows rise in power generation (harvesting) by increasing *L/D* ratio.

By looking into the details of the Figs. 10 and 11, for *L/D* = 1, the RMS value of the voltage is increase d as the gap is increased. Figs. 12 and 13 show the v ariation in RMS voltage with varying length (*L/D*). Th e flag deformation is shown by the black line, for *L/D* = 1 unidirectional bending is observed (Figs. 10 and 11). As the length of the flag is doubled, the bidirecti onal bending is observed as shown by the flag deform ations in the Figs. 12 and 13.

This unidirectional and bidirectional bending causes the low and high energy (voltage). Alike *L/D* = 1 in experimentation, the computed results at *L/D* = 1.25 and 1.5 (Figs. 3 and 6) also show unidirectional bending having low bending energy. As the length is increased to *L/D* = 1.75 in numerical simulations and *L/D* = 2 in the experimentations, bidirectional bending was observed along with the increased energy compared to that at *L/D* = 1, showing that the bi-directional bending phenomenon causes energy augmentation and critical length for the bidirectional bending comes to be *L/D* = 1.75 ~ 2.

4. Conclusions

We examined the dynamics of energy harvesting from a flexible flag behind a D-shaped cylinder undergoing passive flapping subjected to a uniform viscous flow by using the immersed boundary method and wind tunnel testing. The analysis was carried out under varying spacing between the cylinder and flag (*S/D*), the length of the flag (*L/D*) and bending stiffness (γ). For the passive flapping, the increase in bending stiffness for 0.04 ≤ γ ≤ 0.08 and the length ratio of the flag (1.5 ≤ *L/D* ≤ 1.9) cause an increase in the bending energy. The increase in the bending stiffness is accompanied by the increase in the flag deformation as well

as the dominant and the flapping frequency is increased. Constructive mode is observed for the optimal bending energy region when the streamwise distance is increased. The unidirectional curvature is attributed to the low bending energy while the bidirectional curvature is attributed to the high bending energy case. The frequency of the tail flapping is the same for both cases but the amplitude of the tail flapping is different, the amplitude is higher for the high bending energy case and vice versa. The vortex obtained at the tail of the flag has higher energy than the low bending energy case, this depicted the energy harvesting from the upcoming vortices by intercepting while low energy is obtained for the flag passing between the upstream vortices. Similar vortex interception and slaloming mode are observed with the variation of the pitching and the heaving amplitudes. By analyzing the passive flapping we obtained the optimal length of the flag, gap distance between the flag and cylinder and bending rigidity. Experimentation clearly depicts that by increasing streamwise distance between cylinder and flag higher values of voltage were obtained, i.e., electrical energy and similar relation were observed for varying L/D. It was also observed that more power was obtained at higher values of L/D. Higher value of electrical energy is obtained at $L/D = 2$, $Re = 30,000$ and $S/D \geq 3.0$.

Acknowledgements

References

Abdelkefi, A. (2016), "Aeroelastic energy harvesting: A review", *Int. J. Eng. Sci.*, **100**, 112-135.

Allen, J.J. and Smits, A.J. (2001), "Energy harvesting eel", *J. Fluids Struct.*, **15**(3-4), 629-640.

Arthouros, Z. (2014), Renewables 2014 global status report. RENS 21

Barrero-Gil, A., Alonso, G. and Sanz-Andres, A. (2010), "Energy harvesting from transverse galloping", *J. Sound Vib.*, **329**(14), 2873-2883.

Baz, A. and Ro, J. (1991), "Active control of flow induced vibrations of a flexible cylinder using direct velocity feedback", *J. Sound Vib.*, **4**, 313.

Bernitsas, M.M., Raghavan, K., Ben-Simon, Y. and Garcia E.M. (2008), "VIVACE (Vortex Induced Vibration Aquatic Clean Energy): A new concept in generation of clean and renewable energy from fluid flow", *J. Offshore Mech. Arct.*, **130**(4), 041101.

Bin, Q., Alam M.M. and Zhou, Y. (2017), "Two tandem cylinders of different diameter in cross-flow: flow-induced vibration", *J. Fluids Mech.*, **829**, 621-658.

Dai, H.L., Abdelkefi, A. and Wang, L. (2014), "Theoretical modelling and nonlinear analysis of piezoelectric energy harvesting from vortex induced vibrations", *J. Intel. Mat. Syst. Struct.*, **25**, 1861.

Eldredge, J.D. (2008), "Dynamically coupled fluid–body interactions in vorticity-based numerical simulations", *J. Comput. Phys.*, **227**(21), 9170-9194.

Ge, M. (2016), "Numerical investigation of flow characteristics

over dimpled surface", *Int. J. Therm. Sci.*, **20**(3), 903-906.

Govardhan, R. and Williamson, C.H.K. (2004), "Critical mass in vortex-induced vibration of a cylinder", *Eur. J. Mech. B/Fluids*, **23**, 17.

Grue, J., Asbjørn, M. and Enok, P. (1988), "Propulsion of a foil moving in water waves", *J. Fluid Mech.*, **186**, 393-417.

Hartong, J.P.D. (1984), Mechanical Vibrations, New York: McGraw-Hill

Huang, WX., Shin, S.J. and Sung, H.J. (2007), "Simulation of flexible filaments in a uniform flow by the immersed boundary method", *J. Comput. Phys.*, **226**(2):2206-2228.

Isshiki, H. and Murakami, M. (1984), "A theory of wave devouring propulsion (4th report)", *J. Soc. Naval Archit. Japan*, **156**, 102-114.

Johnson, T. and Patel, V. (1999), "Flow past a sphere up to a Reynolds number of 300", *J. Fluid Mech.*, **378**, 19-70.

Khalak, A. and Williamson, C.H.K. (1997), "Investigation of the relative effects of mass and damping in vortex-induced vibration of a circular cylinder", *J. Wind Eng. Ind. Aerod.*, **69**, 341-350.

Liao, J.C., Beal, D.N., Lauder, G.V. and Triantafyllou, M.S. (2003), "Fish exploiting vortices decrease muscle activity", *Science*, **302**(5650), 1566-1569.

Matsumoto, M. (2005), "Flutter instability of structures", *Proceedings of the 4th European and African conference on wind engineering*, 6-11

Matsumoto, M., Okubo, K., Ito, Y., Matsumiya, H. and Kim, G. (2006), "Fundamental study on the efficiency of flutter power generation system", *Proceedings of the ASME2006 Pressure Vessels and Piping/ICPVT-11 Conference. American Society of Mechanical Engineers.*

McKinney, W. and DeLaurier, J. (1981), "The wingmill: an oscillating-wing windmill", *J. Energy*, **5**(2), 109-115.

Panton, R.L. (2005), Incompressible Flow, Wiley.

Peng, Z. and Qiang, Z. (2009), "Energy harvesting through flow-induced oscillations of a foil", *Phys. Fluids*, **21**(12), 123602.

Sakamoto, H. and Haniu, H., (1990), "A study of vortex shedding from spheres in uniform flow", *J. Fluids Eng.*, **112**, 386-393.

Shoele, K. and Mittal, R. (2016), "Energy harvesting by flow-induced flutter in a simple model of an inverted piezoelectric flag", **790**, 582-606

Singh, K., Sébastien, M. and Emmanuel D.L. (2012), "The effect of non-uniform damping on flutter in axial flow and energy-harvesting strategies", *Proc. R. Soc. A*, **468**(2147), 3620-3635.

Taneda, S. (1978), "Visual observations of the flow past a sphere at Reynolds numbers between 104 and 106", *J. Fluid Mech.*, **85**, 187-192.

Tian, F.B., Luo, H., Zhu, L. and Lu, X.Y. (2011), "Coupling modes of three filaments in side-by-side arrangement", *Phys. Fluids*, **23**, 111903

Triantafyllou, M.S., Alexandra H.T. and Franz S.H. (2004), "Review of experimental work in biomimetic foils", *IEEE J. Oceanic Eng.*, **29**(3), 585-594.

Uddin, E. and Sung, H.J. (2011), "Simulation of flow-flexible body interactions with large deformation", *Int. J. Numer. Meth. Fl.*, **21**(9). 1089-1102.

Uddin, E., Huang, W.X. and Sung, H.J. (2013), "Interaction modes of multiple flexible flags in a uniform flow", *J. Fluid Mech.*, **729**, 563-583.

Uddin, E., Huang, W.X. and Sung, H.J. (2015), "Actively flapping tandem flexible flags in a viscous flow", *J. Fluid Mech.*, **780**, 120-142

van Dyke, M. (1982), An Album of Fluid Motion, Parabolic Press, 28-31.

Wu, T.Y. (1971), "Extraction of flow energy by a wing oscillating in waves", *J. Ship Res.*, 66-78

Wu, T.Y. and Chwang, A.T. (1975), Swimming and flying in

nature, volume 2. Springer Science+Business Media, LLC, New York, NY, USA.

Xu, Y.Q., Wang, M.Y., Liu, Q.Y., Tang, S.Y. and Tian, F.B. (2018), "External force-induced focus pattern of a flexible filament in a viscous fluid", *Appl. Math. Model.*, **53**, 369-383

Zhu, L. (2009), "Interaction of two tandem deformable bodies in a viscous incompressible flow", *J. Fluid Mech.*, **635**, 455-475.

Zhu, Q., Wolfgang, M.J., Yue, D.K.P. and Triantafyllou, M.S. (2002), "Three-dimensional flow structures and vorticity control in fish-like swimming", *J. Fluid Mech.*, **468**, 1-28.